

## X-ray phase contrast with injected gas for tumor microangiography

This content has been downloaded from IOPscience. Please scroll down to see the full text.

2014 Phys. Med. Biol. 59 2801

(<http://iopscience.iop.org/0031-9155/59/11/2801>)

View [the table of contents for this issue](#), or go to the [journal homepage](#) for more

Download details:

IP Address: 130.237.32.230

This content was downloaded on 09/09/2014 at 11:14

Please note that [terms and conditions apply](#).

# X-ray phase contrast with injected gas for tumor microangiography

U Lundström<sup>1</sup>, U K Westermark<sup>2</sup>, D H Larsson<sup>1</sup>, A Burvall<sup>1</sup>,  
M Arsenian Henriksson<sup>2</sup> and H M Hertz<sup>1</sup>

<sup>1</sup> Biomedical and X-Ray Physics, Department of Applied Physics,  
KTH Royal Institute of Technology/Albanova, SE-10691 Stockholm, Sweden

<sup>2</sup> Department of Microbiology, Tumor and Cell Biology (MTC), Karolinska Institutet,  
SE-17177 Stockholm, Sweden

E-mail: [ulf.lundstrom@biox.kth.se](mailto:ulf.lundstrom@biox.kth.se)

Received 28 January 2014, revised 25 March 2014

Accepted for publication 15 April 2014

Published 7 May 2014

## Abstract

We show that the microvasculature of mouse tumors can be visualized using propagation-based phase-contrast x-ray imaging with gas as the contrast agent. The large density difference over the gas–tissue interface provides high contrast, allowing the imaging of small-diameter blood vessels with relatively short exposure times and low dose using a compact liquid-metal-jet x-ray source. The method investigated is applied to tumors (E1A/Ras-transformed mouse embryonic fibroblasts) grown in mouse ears, demonstrating sub-15- $\mu\text{m}$ -diameter imaging of their blood vessels. The exposure time for a 2D projection image is a few seconds and a full tomographic 3D map takes some minutes. The method relies on the strength of the vasculature to withstand the gas pressure. Given that tumor vessels are known to be more fragile than normal vessels, we investigate the tolerance of the vasculature of 12 tumors to gas injection and find that a majority withstand 200 mbar pressures, enough to fill 12- $\mu\text{m}$ -diameter vessels with gas. A comparison of the elasticity of tumorous and non-tumorous vessels supports the assumption of tumor vessels being more fragile. Finally, we conclude that the method has the potential to be extended to the imaging of 15  $\mu\text{m}$  vessels in thick tissue, including mouse imaging, making it of interest for, e.g., angiogenesis research.

Keywords: x-ray, phase-contrast, angiography, tumor, propagation-based, microangiography, gas

(Some figures may appear in colour only in the online journal)

## 1. Introduction

Knowledge concerning the development of new blood vessels, angiogenesis, is essential for understanding the growth, invasion and spread of solid tumors. Basic research, as well as the assessment of novel therapies, benefit from analyses of local tumor angiogenesis. Unfortunately, the available techniques for the imaging of the intact microvasculature limit progress since they do not have sufficient spatial resolution to allow observation of the finer blood vessels (McDonald and Choyke 2003). Such high-resolution microangiography is of importance for diverse studies in mouse-based pre-clinical models including initiation, development and growth of tumor vessels (Carmeliet and Jain 2000), the morphology of tumor vasculature (McDonald and Choyke 2003, Carmeliet and Jain 2000), microvascular density measurements (McDonald and Choyke 2003, Cox *et al* 2000), and quantification of the anti-angiogenic effect of inhibitors (McDonald and Choyke 2003, Savai *et al* 2009). To date, several therapies based on angiogenic inhibitors are in use or have been evaluated clinically (Folkman 2006, Ebos and Kerbel 2011, Carmeliet and Jain 2011).

Present techniques for small-animal angiography include magnetic resonance imaging (Bolan *et al* 2006), single photon-emission computed tomography, positron emission tomography (PET) (Gambhir 2002), ultrasonography (Ogura *et al* 2001) and laboratory-based x-ray tomography (Kiessling *et al* 2004, Clark *et al* 2013). They all have insufficient resolution, 50–100  $\mu\text{m}$  to mm, to image the smaller vessels. Optical methods such as confocal microscopy, multi-photon microscopy (Maurin *et al* 2011) and optical coherence tomography (Vakoc *et al* 2012) have higher resolution but are limited to a relatively thin region closest to the surface. Very high-resolution imaging ( $<10 \mu\text{m}$ ) of the microvasculature of mouse tumors using x-ray absorption-contrast agents has been demonstrated at synchrotrons (Chien *et al* 2012, Chien *et al* 2010), but the availability of these large facilities is limited and the required radiation dose using absorption contrast is incompatible with longitudinal studies.

In the present paper we demonstrate that laboratory x-ray phase contrast allows the imaging of the microvasculature of tumors at the sub-15- $\mu\text{m}$  vessel level. The method relies on propagation-based x-ray phase-contrast imaging (Wilkins *et al* 1996) with injected gas as contrast agent (Lundström *et al* 2012b). The use of injected gas suggests a potential path to *in vivo* experiments with  $\text{CO}_2$  as the gas (Cho and Hawkins 2007, Lundström *et al* 2012b). In normal tissue our phase-contrast method has been shown to provide sufficient contrast to image sub-10- $\mu\text{m}$ -diameter vessels with reasonable exposure times with a compact liquid-metal-jet x-ray source (Lundström *et al* 2012a). Here we extend the method to blood vessels in tumorous tissue, demonstrating imaging in sub-15- $\mu\text{m}$ -diameter vessels. The tumors were grown in mouse ears and imaged both in 2D projection imaging and 3D tomography shortly after the mice had been sacrificed. Of special importance for the applicability of the method is the resistance of the blood vessels in tumors to the elevated gas pressures, since such vessels are generally known to be more fragile than vessels in normal tissue. We show that tumor vasculature with vessels less than 15  $\mu\text{m}$  in diameter can be gas-filled at injection pressures tolerated by the tumor vessels.

## 2. Materials and methods

Tumors were grown by injecting  $1 \times 10^5$  E1A/Ras-transformed mouse embryonic fibroblasts (Wilhelm *et al* 2010) in  $\sim 10 \mu\text{l}$  cell culture media without antibiotics above the cartilage plane of the ear (Li *et al* 2012) in anesthetized athymic-Nude-FOXN1<sup>nu</sup> mice. Tumors developed within two weeks of injections and had an average diameter of 2.1 mm with a standard deviation of 0.6 mm. All animal experiments were in accordance with the Animal

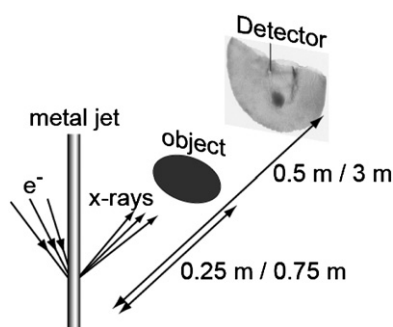


**Figure 1.** Propagation-based phase-contrast x-ray imaging uses a magnifying projection arrangement with the propagation distance turning phase shifts into intensity variations. Imaging was done in two modes with different imaging distances as indicated in the figure.

Protection Law (SFS1988:534), the Animal Protection Regulation (SFS1988:539) and the Regulation for the Swedish National Board for Laboratory Animals (SFS1988:541) and were approved by the Stockholm regional ethics committee for animal research under ethical permit N283/12.

To achieve a high contrast in the phase-contrast images, air was injected into the vascular system. For this proof-of-principle study air was used instead of CO<sub>2</sub> gas, as in previous studies, for convenience since the type of gas does not affect the image contrast. We first removed the ear from the freshly euthanized mouse and then inserted a needle directly into the largest vein. This was done under a microscope with the needle held by a manual three-axis micrometer stage. To prevent gas from leaking out around the needle the vessel was sealed with a small drop of tissue glue (Gluture, World Precision instruments). Four different needles were used: a 36-gauge beveled steel needle, a 36-gauge blunt steel needle, a glass capillary and a polycarbonate tube. The steel needles had an outer diameter (OD) of 115  $\mu\text{m}$  and an inner diameter (ID) of 40  $\mu\text{m}$ , the glass capillary had OD 120  $\mu\text{m}$  and ID 80  $\mu\text{m}$  and the plastic tube had OD 50  $\mu\text{m}$  and ID 33  $\mu\text{m}$ . The needles had different advantages and disadvantages but all worked. The beveled steel needle was easier to insert into a vessel than the blunt one but could cut through the vessel wall once inserted. The glass capillary was as difficult to insert as the blunt steel needle but required a lower gas pressure for initial injection due to the larger inner diameter. The plastic tube was most readily inserted due to its smaller OD, but required slightly higher pressure for initial injection due to its smaller inner diameter. The gas pressure was continuously measured and automatically controlled by a syringe pump.

For imaging we used a liquid-metal-jet x-ray source (Hemberg *et al* 2003) similar to the one described by Larsson *et al* (2011), but with Galinstan (GaInSn alloy) as the anode material (Excillum AB). It was operated with an acceleration voltage of 50 kV and 0.8 mA of e-beam current (40 W of power), with an approximately  $7 \times 7 \mu\text{m}^2$  x-ray spot measured as the full width at half maximum. The 9.25 keV gallium K $\alpha$  line dominates the x-ray spectrum and is the main contributor to the images.

Propagation-based phase-contrast x-ray images were obtained in two modes as is shown in figure 1. The short-distance mode with a source-to-object distance of 0.25 m and a source-to-detector distance of 0.5 m was used for figures 2 and 4. The long-distance mode with the distances 0.75 m and 3 m, respectively, was used for figure 3. The short mode has a low magnification making the full ear fit within the field of view. The long mode gives higher resolution and stronger phase contrast, which allows for lower-dose imaging. The long mode

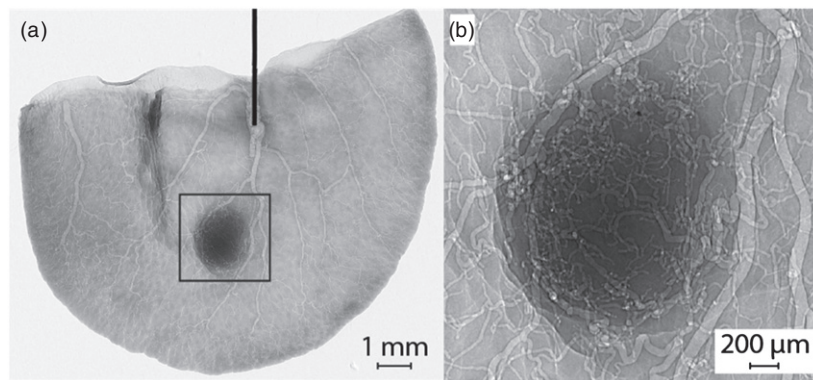


**Figure 2.** Projection image of a mouse ear with a tumor imaged with source-to-object distance 0.25 m and magnification 2. Image of the full ear (a) (with the tumor marked by a rectangle) and (b) a zoom-in on the tumor. The venous system is filled with air at a pressure of 200 mbar. Many of the smaller vessels are below  $15\ \mu\text{m}$  in diameter.

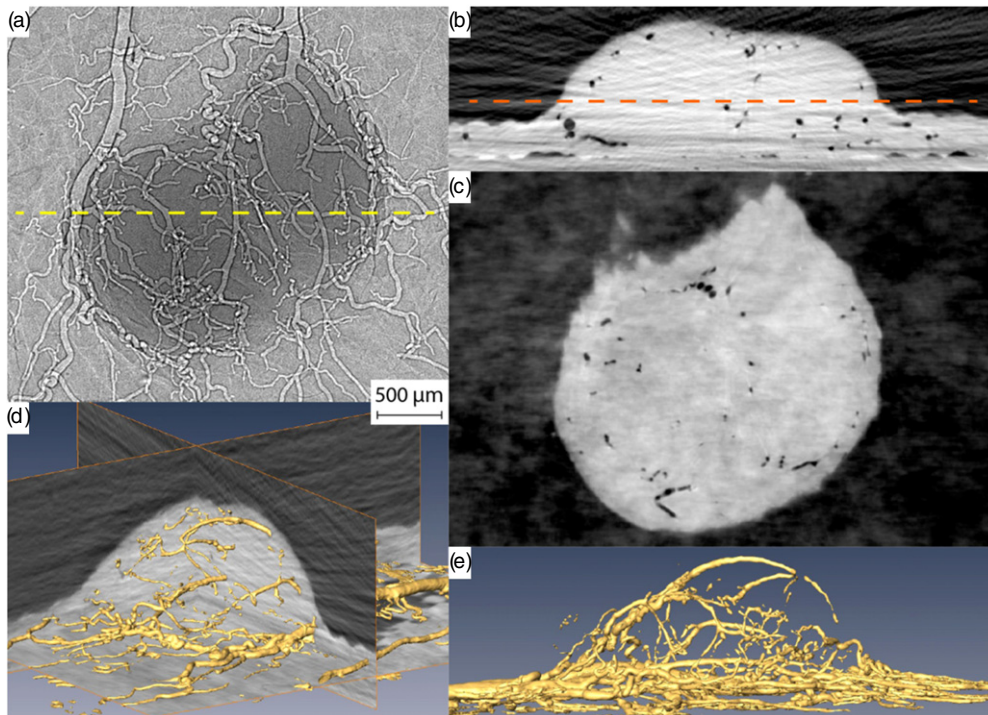


**Figure 3.** Tomography of a mouse ear tumor. (a) A single 20 s (40 mGy) projection image. (b) A section corresponding to the dashed line in (a) in the tomographic reconstruction of the tumor. (c) A section corresponding to the dashed line in (b). (d), (e) Iso-surface in the reconstruction. The tomogram had a total exposure time of 7.5 min giving a radiation dose of about 1 Gy. A larger magnification ( $4\times$ ) and source-to-object distance (0.75 m) compared to figure 2 were used to boost the contrast and lower the radiation dose. The scale bar applies to all figure panels.

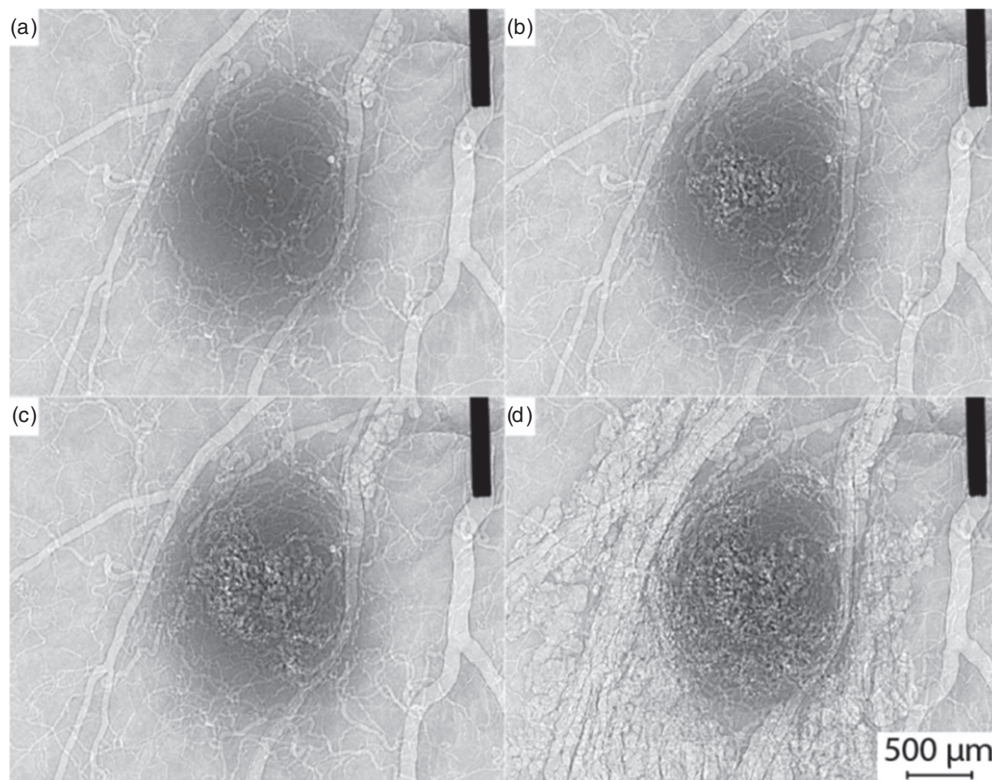


**Figure 4.** Breaking of tumor vasculature. A mouse tumor just before breaking (a), 1 min later (b), 2 min later (c) and 10 min later (d). A vessel in the tumor breaks, letting gas out into the tissue. The gas pressure opens up the tissue letting more gas out. Eventually the breaking spreads outside the tumor and throughout the ear. The black rectangle is the needle used to inject gas.

requires evacuated flight tubes to be inserted into the x-ray beam path to reduce air absorption of the 9.25 keV radiation. The detector is a Photonic Science  $24 \times 36 \text{ mm}^2$  CCD with  $9 \mu\text{m}$  pixels fiberoptically coupled 1:1 to a  $5 \text{ mg cm}^{-2}$  Gadox scintillator. The projection images shown have exposure times of 10 s (figure 4), 20 s (figure 3) and 40 s (figure 2) in order to obtain very low noise levels. However, in all cases about 2 s of exposure is enough to detect all gas-filled vessels. Radiation doses are calculated from the mass energy-attenuation coefficients from NIST (Hubbell and Seltzer 2011) as the average dose deposited in a  $200 \mu\text{m}$  thick piece of soft tissue corresponding to the ear. The average dose in the tumor will be slightly lower due to its thickness. The short mode has a dose rate of about  $20 \text{ mGy s}^{-1}$  and the long mode  $2.4 \text{ mGy s}^{-1}$ .

Tomographic data sets were obtained by rotating the object around a vertical axis. Each mouse ear was attached to a  $200 \mu\text{m}$  thick plastic (PET) sheet with double adhesive tape to keep it stable during tomography. We used 90 projection images over  $180^\circ$  with 5 s exposure time each, giving a total exposure time of 7.5 min and a dose of 400 mGy. The images were binned  $2 \times 2$  during CCD readout giving  $18 \times 18 \mu\text{m}^2$  pixels and a total acquisition time of 9 min including readout time for the CCD. Reconstructions were made using filtered back projection in cone-beam geometry with the Octopus software package (Vlassenbroeck *et al* 2007). Before reconstruction the images were phase retrieved (Burvall *et al* 2011) using

an algorithm by Paganin *et al* (2002) to obtain the projected density of the object from the phase-contrast images.

The sizes of vessels that were gas-filled were measured to evaluate the filling process. This was done in a semiautomatic way. For each gas pressure level at which a tumor was imaged, we manually marked the locations and directions of straight sections of the smallest non-overlapping vessels (on average 30 vessels per image). A program obtained an intensity profile of each vessel by averaging along the vessel and then compared this to simulated profiles of vessels of various diameters and slight variations in position to find the best fit. The diameter down to which the vascular system was said to be filled is taken as the average of the five smallest vessels found in each image. The simulations were performed using a wave-propagation algorithm taking into account all important imaging parameters including source size and spectrum, detector point spread function and detector absorption efficiency as described by Lundström *et al* (2012b). Most marked vessels were outside the tumors since these were straighter and overlapped other vessels less often, but the smallest vessels in the tumors appear to be of the same diameters as those outside. The same method was used to determine changes in vessel diameter over time, but then a set of vessels in the tumor and another set in the healthy tissue were marked in one image. The same vessels were then automatically measured in several images taken over the following 30 min.

### 3. Results

The imaging of tumor vasculature could be done in a manner similar to healthy vasculature (Lundström *et al* 2012a), except for two differences. First, tumor vessels are more fragile than normal vessels and hence break more easily than vessels in the surrounding tissue. This limits the gas pressure that can be applied and, thus, increases the lower limit on the size of vessels being gas-filled. Second, the large number of vessels in the periphery of the tumor makes projection images difficult to interpret. This necessitates the use of tomography to get a 3D image of the vasculature.

Figure 2 shows an example of a tumor in a mouse ear injected with air at a gauge pressure of 200 mbar imaged using the short-distance mode. The vascular network is easily traced throughout the ear out to the 15  $\mu\text{m}$  vessels which are the smallest ones being gas filled. Tracing the vessels gets somewhat more difficult in the tumor because of the large number of overlapping vessels. Nevertheless, the overall structure can be seen and most vessels seem to be confined to the borders of the tumor.

Figure 3 shows a tumor on which we also performed tomography. Here we used the long-distance mode to get a stronger phase contrast and lower radiation dose. 90 images and a 5 s exposure time per image was used to get a quick tomogram with low dose. Some streak artifacts appear in the directions close to being parallel to the plane of the ear. These are caused by the high absorption in the parts of the ear outside the field of view in combination with the low number of projection angles used. They could potentially be alleviated with a higher number of projections or using an iterative reconstruction algorithm that is less susceptible to angular undersampling. The high contrast of the vessels, however, still makes all of them clearly visible and segmentable (figures 3(d), (e)). This tumor consists of two nodules, with almost all the vessels either close to the tumor surface or at the interface between the two nodules (figures 3(b), (c)). In figure 3(e) we can observe how these vessels protrude from the plane of vessels associated with the healthy ear. The 3D renderings were made with the Amira software package (Visualization Science Group). The iso-surface corresponds to a threshold density of about  $0.5 \text{ g cm}^{-3}$  and the surfaces toward the outside air removed. Figure 3(d) also includes three orthogonal sections of the tumor.

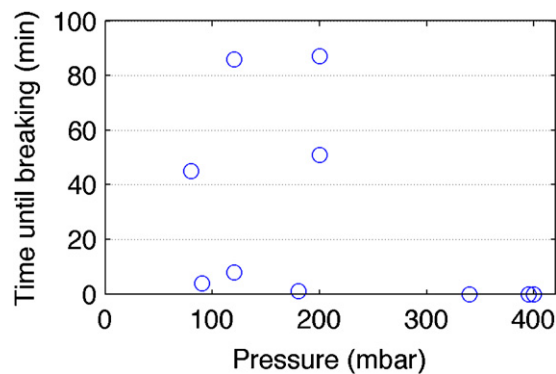


**Figure 5.** Time until vessel breakage. At pressures up to 200 mbar, four out of seven tumors held up for more than 40 min, more than enough to acquire a good tomogram. At pressures above 300 mbar all three tumors broke immediately.

Using this imaging method we can clearly visualize the disorganized vascular architecture typical for tumors (Folarin *et al* 2010). Tortuous vessels feed into the tumor from the surrounding normal tissue forming an immature and poorly organized vasculature with shunts and blind endings (figures 2(b), 3(a)) indicative of a strong angiogenic response generated by the tumor.

Tumor vasculature is known to be more chaotic and permeable than normal vasculature (Siemann 2011) so the fact that it breaks more easily from an elevated internal pressure is not surprising. When this happens gas penetrates into the surrounding tissue, breaking it up in a way that spreads throughout the tumor and ear. Figure 4 shows a sequence of images at different stages of this breaking process. Breaking always started in the tumor, except for in one case where the largest vessel where the gas was injected broke.

The time it took from injection of gas until the vessels broke varied between tumors from less than a minute up to more than an hour. This is plotted in figure 5, with the applied gas pressure on the horizontal axis. It seems reasonable that a higher pressure would give a shorter time. The variability of the tumors seems to hide such a trend in our data, except for pressures above 300 mbar at which all three tumors broke immediately. A majority of the tumors for which the pressure was up to 200 mbar took more than 40 min before breaking, giving plenty of time for imaging.

Figure 6 shows the diameters of the smallest vessels that were filled with gas in the tumor images. The data support that the minimum vessel diameter  $D$  depends on the applied gas pressure  $P$  as  $D = 4\gamma/P$ , where  $\gamma = 60 \text{ mN m}^{-1}$  is the surface tension of blood at room temperature. This curve is similar to previous experiments in normal non-tumor vessels (Lundström *et al* 2012a) but with lower maximum pressure, reflecting the more fragile nature of the tumor vasculature. Thus, it appears that  $12 \mu\text{m}$  vessels can be filled with 200 mbar of gas pressure. Two ears were excluded from figures 5 and 6 since we suspected partial blocking of the needle opening in those cases. For one of those ears, 700 mbar was required to inject any gas and for the other only the three largest vessels filled at 130 mbar. In the three cases of immediate vessel rupture (above 300 mbar) the vessel sizes could not be determined. Some ears were imaged at two or three gas pressures and appear as multiple data points in figure 6. The two data points at 200 mbar depicting minimum vessel sizes above the theoretical are assumed to have a partial blocking of the injection needles giving a lower pressure in the vessels than in the syringe.

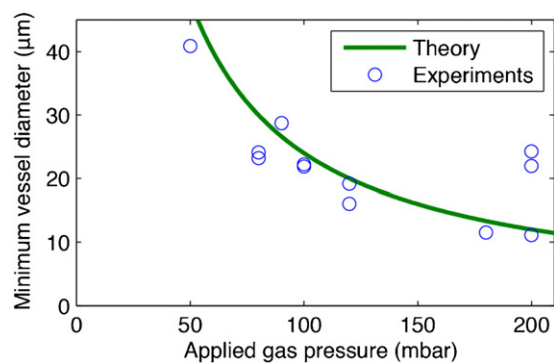


**Figure 6.** The smallest vessel size observed plotted versus applied gas pressure. The solid line corresponds to the minimum vessel diameter expected at surface tension equilibrium and the circles correspond to measured minimum diameters in images acquired at different injection pressures.

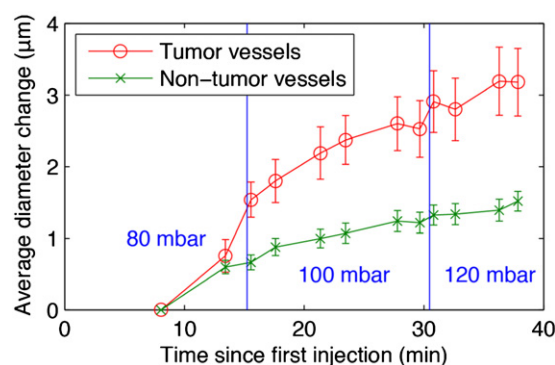


**Figure 7.** Time development of vessel diameters for tumor and non-tumor vessels. For all images the diameter is compared to the diameter in the image taken 8 min after first injection. Error bars indicate the standard uncertainty in the average diameter change.

Since propagation-based phase contrast enhances high spatial frequencies and therefore edges, vessel diameters can be measured with high accuracy. We use this to measure how the vessels are affected by the gas pressure by imaging a tumor regularly while increasing the pressure in steps. A set of 109 non-tumor vessels and 37 tumor vessels were manually marked in one first image and then automatically measured in all subsequent images with increasing pressure. Figure 7 shows how the average diameter of the vessels developed over time. Non-tumor vessels expanded on average by  $1.6 \mu\text{m}$  over a 30 min period exposed to a gas pressure that was increased from 80 to 120 mbar. Tumor vessels on the other hand expanded twice as much, by  $3.2 \mu\text{m}$ , over the same time span. Larger vessels expanded slightly more than smaller ones. The selected non-tumor vessels above  $50 \mu\text{m}$  expanded on average by  $1.9 \mu\text{m}$  while those below expanded by  $1.6 \mu\text{m}$ . Since the tumor only contained vessels up to about  $50 \mu\text{m}$  in diameter only the non-tumor vessels up to this diameter were used in the comparison in figure 7.

The larger increase in diameter of the tumor vessels is probably linked to our previous finding that tumor vessels break more easily than vessels in normal tissue. The cause is in both cases likely to be the weaker vessel walls in tumors. The expansion of a vessel is probably a

first step toward its breaking since it will increase the force exerted by the internal pressure and at the same time weaken the vessel wall.

The distributions of diameter changes overlap considerably between tumor and non-tumor vessels. This is likely due to internal variations between vessels and inaccuracies in the measurements caused by photon noise and overlapping structures. Some vessels labeled as tumor vessels might also belong to the healthy tissue behind or in front of the tumor in the projection images. The error bars indicate the uncertainty of the average change calculated as  $u = \frac{\sigma}{\sqrt{N}}$ , where  $\sigma$  is the standard deviation among the diameter changes and  $N$  is the number of diameter changes used.

#### 4. Discussion

It has previously been shown that gas can be used as a contrast agent in phase-contrast x-ray imaging of mice allowing visualization of sub-10- $\mu\text{m}$  blood vessels in normal tissue at reasonable exposure times and radiation doses (Lundström *et al* 2012a). Here we demonstrate that the method also is applicable to the imaging of the microvasculature of tumors. The tumor vessels are more sensitive to the gas pressure than the surrounding vasculature, but still for more than half of the tumors exposed to up to 200 mbar of gas pressure the vessels stayed intact for more than 40 min. This provides ample time to acquire a good tomogram, and 200 mbar is enough to fill 12  $\mu\text{m}$  vessels with gas. In addition, the method can be used to measure vessel wall elasticity and compliance by observing the change in vessel diameter over time and when changing the gas pressure.

In this study the tumors were placed in mouse ears to get short exposure times and to avoid distracting the surrounding tissue. However, there is no principal reason why the same procedure would not work for tumors in other organs as well. Previously, this method has been shown to work well for 10 mm thick samples (Lundström *et al* 2012b), and simulations following our earlier protocol (Lundström *et al* 2012b) show that for the 20 mm thickness of a full mouse, visualization of 10  $\mu\text{m}$  vessels would require approximately a 1 h exposure time using present technology.

In this study gas was injected into the venous system, mainly because the largest arteries were too small (of the order of 25  $\mu\text{m}$  in diameter) for us to manage gas injection. Arteries and arterioles have considerably stronger vessel walls than veins and venules, so they should withstand the gas pressure better. It is thus likely that higher gas pressures than those used in this study can be used for arterial systems for thicker tissues, where the arteries are large enough for injection.

Finally, we note that it appears feasible to use the method for *in vivo* studies, provided that a dissolvable gas such as carbon dioxide is used as contrast agent. Carbon dioxide is already employed clinically for angiography (Cho and Hawkins 2007) and was also used in previous phase-contrast studies (Lundström *et al* 2012b). Tomography seems practically feasible only for body parts like an ear that can be held firmly in place, with single projections being more realistic for the rest of the animal.

#### Acknowledgments

We thank Dr M Wilhelm, Karolinska Institutet, for generously providing the transformed mouse embryonic fibroblasts used for tumor inoculation. This work was supported by the Swedish Research Council, the Swedish Cancer Society and the Wallenberg Foundation.

## References

- Bolan P J, Yacoub E, Garwood M, Ugurbil K and Harel N 2006 *In vivo* micro-MRI of intracortical neurovasculature *Neuroimage* **32** 62–9
- Burvall A, Lundström U, Takman P A C, Larsson D H and Hertz H M 2011 Phase retrieval in x-ray phase-contrast imaging suitable for tomography *Opt. Express* **19** 10359–76
- Carmeliet P and Jain R K 2000 Angiogenesis in cancer and other diseases *Nature* **407** 249–57
- Carmeliet P and Jain R K 2011 Molecular mechanisms and clinical applications of angiogenesis *Nature* **473** 298–307
- Chien C-C, Chen H-H, Lai S-F, Hwu Y, Petibois C, Yang C, Chu Y and Margaritondo G 2012 X-ray imaging of tumor growth in live mice by detecting gold-nanoparticle-loaded cells *Sci. Rep.* **2**
- Chien C-C, Wang C, Wang C, Li E, Lee K, Hwu Y, Lin C-Y, Chang S-J, Yang C and Petibois C 2010 Synchrotron microangiography studies of angiogenesis in mice with microemulsions and gold nanoparticles *Anal. Bioanal. Chem.* **397** 2109–16
- Cho K and Hawkins I F 2007 *Carbon Dioxide Angiography* (London: Informa Healthcare)
- Clark D P, Ghaghada K, Moding E J, Kirsch D G and Badea C T 2013 *In vivo* characterization of tumor vasculature using iodine and gold nanoparticles and dual energy micro-CT *Phys. Med. Biol.* **58** 1683
- Cox G, Walker R, Andi A, Steward W and O'Byrne K 2000 Prognostic significance of platelet and microvessel counts in operable non-small cell lung cancer *Lung Cancer* **29** 169–77
- Ebos J M and Kerbel R S 2011 Antiangiogenic therapy: impact on invasion, disease progression, and metastasis *Nature Rev. Clin. Oncol.* **8** 210–21
- Folarin A, Konerding M, Timonen J, Nagl S and Pedley R 2010 Three-dimensional analysis of tumour vascular corrosion casts using stereoinaging and micro-computed tomography *Microvasc. Res.* **80** 89–98
- Folkman J 2006 Angiogenesis *Annu. Rev. Med.* **57** 1–18
- Gambhir S S 2002 Molecular imaging of cancer with positron emission tomography *Nature Rev. Cancer* **2** 683–93
- Hemberg O, Otendal M and Hertz H M 2003 Liquid-metal-jet anode electron-impact x-ray source *Appl. Phys. Lett.* **83** 1483–5
- Hubbell J H and Seltzer S M 2004 Tables of x-ray mass attenuation coefficients and mass energy-absorption coefficients from 1 keV to 20 MeV for elements Z = 1 to 92 and 48 additional substances of dosimetric interest (version 1.4) (Gaithersburg, MD: National Institute of Standards and Technology) (<http://physics.nist.gov/xaamdi>)
- Kiessling F *et al* 2004 Volumetric computed tomography (VCT): a new technology for noninvasive, high-resolution monitoring of tumor angiogenesis *Nature Med.* **10** 1133–8
- Larsson D H, Takman P A C, Lundström U, Burvall A and Hertz H M 2011 A 24 keV liquid-metal-jet x-ray source for biomedical applications *Rev. Sci. Instrum.* **82** 123701
- Li J L, Goh C C, Keeble J L, Qin J S, Roediger B, Jain R, Wang Y, Chew W K, Weninger W and Ng L G 2012 Intravital multiphoton imaging of immune responses in the mouse ear skin *Nature Protoc.* **7** 221–34
- Lundström U, Larsson D H, Burvall A, Scott L, Westermarck U, Wilhelm M, Henriksson M A and Hertz H M 2012a X-ray phase-contrast CO<sub>2</sub> angiography for sub-10 μm vessel imaging *Phys. Med. Biol.* **57** 7431
- Lundström U, Larsson D H, Burvall A, Takman P A C, Scott L, Brismar H and Hertz H M 2012b X-ray phase contrast for CO<sub>2</sub> microangiography *Phys. Med. Biol.* **57** 2603
- Maurin M, Stephan O, Vial J-C, Marder S R and van der Sanden B 2011 Deep *in vivo* two-photon imaging of blood vessels with a new dye encapsulated in pluronic nanomicelles *J. Biomed. Opt.* **16** 036001
- McDonald D M and Choyke P L 2003 Imaging of angiogenesis: from microscope to clinic *Nature Med.* **9** 713–25
- Ogura O, Takebayashi Y, Sameshima T, Maeda S, Yamada K, Hata K, Akiba S and Aikou T 2001 Preoperative assessment of vascularity by color Doppler ultrasonography in human rectal carcinoma *Dis. Colon Rectum* **44** 538–46
- Paganin D, Mayo S C, Gureyev T E, Miller P R and Wilkins S W 2002 Simultaneous phase and amplitude extraction from a single defocused image of a homogeneous object *J. Microsc.* **206** 33–40
- Savai R, Langheinrich A C, Schermuly R T, Pullamsetti S S, Dumitrascu R, Traupe H, Rau W S, Seeger W, Grimminger F and Banat G A 2009 Evaluation of angiogenesis using micro-computed tomography in a xenograft mouse model of lung cancer *Neoplasia* **11** 48

- Siemann D W 2011 The unique characteristics of tumor vasculature and preclinical evidence for its selective disruption by tumor-vascular disrupting agents *Cancer Treat. Rev.* **37** 63–74
- Vakoc B J, Fukumura D, Jain R K and Bouma B E 2012 Cancer imaging by optical coherence tomography: preclinical progress and clinical potential *Nature Rev. Cancer* **12** 363–8
- Vlassenbroeck J, Dierick M, Masschaele B, Cnudde V, Van Hoorebeke L and Jacobs P 2007 Software tools for quantification of x-ray microtomography at the UGCT *Nucl. Instrum. Methods A* **580** 442–5
- Wilhelm M T, Rufini A, Wetzel M K, Tsuchihara K, Inoue S, Tomasini R, Itie-Youten A, Wakeham A, Arsenian-Henriksson M and Melino G 2010 Isoform-specific p73 knockout mice reveal a novel role for  $\Delta Np73$  in the DNA damage response pathway *Genes Dev.* **24** 549–60
- Wilkins S W, Gureyev T E, Gao D, Pogany A and Stevenson A W 1996 Phase-contrast imaging using polychromatic hard x-rays *Nature* **384** 335–8